

Article

On the Feasibility of Interhemispheric Patch Detection Using Ground-Based GNSS Measurements

Rafal Sieradzki *  and Jacek Paziewski Institute of Geodesy, University of Warmia and Mazury in Olsztyn, 10-719 Olsztyn, Poland;
jacek.paziewski@uwm.edu.pl

* Correspondence: rafal.sieradzki@uwm.edu.pl

Received: 30 October 2018; Accepted: 12 December 2018; Published: 16 December 2018



Abstract: Dual-frequency GNSS data processing is currently one of the most useful techniques for sounding the ionosphere. Hence, this work was aimed at the evaluation of ground-based GNSS data for the continuous monitoring of polar patches in both hemispheres. In this contribution, we proposed to use epoch-wise relative STEC values in order to detect these structures. The applied indicator is defined as a difference between an undifferenced geometry-free linear combination of GNSS signals and the background ionospheric variations, which were assessed with an iterative algorithm of four-degree polynomial fitting. The occurrence of patches during the St. Patrick geomagnetic storm was performed for validation purposes. The first part of the work confirmed the applicability of the relative STEC values for such investigations. On the other hand, it also revealed the limitations related to the inhomogeneous distribution of stations, which may affect the results in both hemispheres. This was confirmed with a preliminary cross-evaluation of GNSS and in situ SWARM datasets. Apart from the periods with a well-established coincidence, the opposite situation, when both methods indicated different parts of the polar ionosphere, was also observed. The second part of this contribution depicted the feasibility of continuous patch detection for both regions, and thus the interhemispheric comparison of the analyzed structures. It has demonstrated the strong disproportion between patches in the northern and southern hemispheres. This discrepancy seems to be related to the different amount of plasma propagating from the dusk sector, which is justified by the values of relative STEC at mid-latitudes. The observed structures are also strongly dependent on the orientation of the interplanetary magnetic field.

Keywords: GNSS; ionosphere; polar patches

1. Introduction

The polar and subpolar areas are characterized by an extremely complicated and dynamic ionospheric structure. It is mainly related to the shape of the geomagnetic field, which allows the transfer of solar wind energy into the ionosphere-magnetosphere system and its dissipation into the ionized part of the atmosphere. Furthermore, these processes are driven by the interplanetary magnetic field (IMF), which is the magnetic field of the Sun frozen into the solar wind flux. It is well-recognized that the particular components of IMF vectors (B_x , B_y —parallel to the ecliptic, toward the Sun, and east–west directions, respectively, B_z —perpendicular to the ecliptic) have different impacts on the ionospheric conditions in polar and auroral regions. The strongest activity of the ionosphere occurs for the southwardly-oriented B_z . It is related to the magnetic reconnection as well as the two-cell pattern of high-latitude plasma convection for such IMF conditions. The former factor is conducive to the growth of particle precipitation, whereas the latter enables feeding the polar ionosphere by the dense stream of plasma from mid-latitudes. As a consequence of both of these processes, the high-latitude ionosphere is affected by the different-scale irregularities with sizes ranging from decameter to several

hundreds of kilometers [1–5]. The impact of the remaining IMF components is much less significant. Nevertheless, it is known that variations of B_y influence the shape of the convection pattern, which in turn modulates the trajectory of polar structures [6].

Polar patches are defined as islands of F-region high-density plasma in a low-density environment with a horizontal size of up to 1000 km. The foreground-to-background ratio for these structures ranges from two to 10, where the lower limit is usually adopted as a detection threshold. The occurrence of polar patches was preliminarily studied with photometer and ionosonde measurements [7,8]. Subsequently, such analyses were extended, taking advantage of ground-based GNSS data [9,10], incoherent scatter radar [11], and in situ measurements [12]. The initial results confirmed the propagation of these structures from the dayside ionosphere across the polar cap with velocities of 400–1000 m/s. Furthermore, the studies reported that patches exiting from the polar cap fed the auroral oval (also called auroral blobs) and flow in the sunward direction according to the high-latitude convection pattern [13–15].

The further studies considered the origin of the patches and mechanism fracturing the plasma. They confirmed that the primary source of high-density plasma is a reservoir at sub-auroral middle latitudes, which are a result of solar EUV radiation [16–19]. During the storms, the signature of this reservoir, extending from the dusk sector of mid-latitudes to the dayside polar cap, is often referenced as storm-enhanced density (SED) [20,21]. The patch generation was also associated with particle precipitation [22]. However, this process can be responsible only for weak patches, up to an equivalent of 5 MHz for foF2 [4,23]. A few explanations have been proposed with regard to the mechanisms responsible for plasma segmentation. The contributions [24,25] linked the patch generation with the temporal variations in IMF B_y and IMF B_z . In [22], it was suggested that this process is related to high-speed flow channel events, while [16] explained it by transient magnetopause reconnection. Although patch generation seems to still be an open issue, the recent studies [26,27] showed good agreement between the latter method and observed patches.

The significance of patches on the appropriate modeling of the polar cap ionosphere was also the reason for detailed climatological studies performed with different techniques, such as: in situ data from low Earth orbit (LEO) satellites (Dynamics Explorer 2, DMSP and SWARM) [6,28], Halley HF radar data [29] and spaceborne GNSS measurements derived from the CHAMP satellite [30]. It was confirmed that daily patch modulation occurs with the greatest frequency at 10:00–22:00 UT and 10:00–23:00 UT in the northern and southern hemispheres, respectively [28,29]. The studies [6,30] were aimed at an interhemispheric comparison of patch appearance. The results given there are consistent with the maximum of patches that was detected during wintertime for the northern hemisphere. On the other hand, there is no agreement for the southern one, where maxima were observed in the local summer and winter, respectively. This discrepancy was preliminarily explained by the distinct definition of patch (related to different measured values, i.e., plasma density and slant total electron content—STEC [31]), and the areas that were used for their detection.

As shown in recent studies aimed at total electron content (TEC) fluctuation [32–34], the current distributions of permanent GNSS stations allow the interhemispheric detection of high-latitude ionospheric disturbances. Thus, one can consider extending patch analyses with this technique. Up to now, GNSS-based investigations of these polar structures were predominantly performed with regional TEC maps [35,36], but this methodology has a number of limitations. The first of them is the temporal resolution of maps, which is not high enough to capture the dynamic structures. The second, even more problematic limitation is the lack of geometrical dependency of STEC patch enhancement on elevation angle [30,37]. As a result, the application of any mapping function used for vertical TEC modeling implicates the distortion of structures in the final ionospheric maps of the ionosphere. In order to overcome these limitations, we propose using relative STEC values derived from a time series of geometry-free combination (L_4). This approach is, to some extent, similar to that applied by [30], where patches were found arc by arc. The parameter applied in our case—the relative STEC value—is the difference between a L_4 combination of GNSS signals at each epoch and the background

STEC level. In order to compute the latter, we used an iterative algorithm of four-degree weighted polynomial fitting applied to arcs of L_4 combination data. The utilization of epoch-wise relative enhancement as a parameter allows following the convections of large-scale ionospheric structures in multi-station mode. The evaluation of the proposed methodology was performed for the St. Patrick storm in March 2015.

The paper is organized as follows. The second section presents a brief description of the algorithm that was used to determine the relative STEC values and the data set that was used in experiment. Subsequently, the conditions during the test period are characterized. This was followed by the core section presenting and discussing the results. The section begins with the characteristics of the spatial distribution of GNSS data in both hemispheres, and the applicability of the proposed methodology for patch convection monitoring. This includes also the initial comparison of GNSS-based results with those from the SWARM satellites. The second part of the section analyzes the temporal occurrence of patches and its dependence on geomagnetic conditions. Finally, the summary and conclusions are given in the last section.

2. Methodology and Data Set

As previous studies showed, the time series of L_4 measurements and relative STEC values can be successfully used for the detection of ionospheric disturbances [38–41]. Considering the polar patches, such approach was applied for particular arcs only [9,14]. In this paper, we provided an algorithm aimed at the combined processing of network-derived observations in order to extend GNSS-based analyses of a high-latitude ionosphere.

The computation of relative STEC values is realized in two steps. The first one is the detection and repair of phase cycle-slips, which frequently occur at high latitudes [5,42]. Initially, we implemented the modified algorithm proposed in [43], which assumes searching and repairing phase cycle-slips using the difference between real and approximated rates of TEC values. However, the preliminary analysis for the southern hemisphere data indicated that the real change of STEC (without cycle-slip) can reach even 15 TECu/min (see Figure 1), and setting up such a high threshold limit led to the unstable work of the algorithm. Hence, we decided to perform a cleaning of the L_4 data using their leveling with code one, according to the equation:

$$\tilde{L}_4(k) = L_4(k) - \text{median}(L_4(k) + P_{4(k)})_{arc} \quad (1)$$

where $\tilde{L}_4(k)$, $L_4(k)$, and $P_{4(k)}$ correspond to the shifted phase, phase, and code data at epoch k , respectively. Due to the opposite sign of the ionospheric effect in both types of observations, the factor in brackets contains the constant term (differences of ambiguities and hardware delays on both frequencies) and the median of noise.

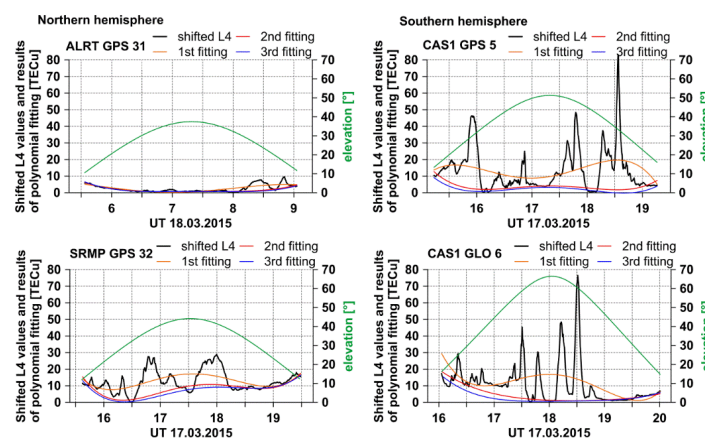


Figure 1. Background slant total electron content (STEC) estimation using iterative polynomial fitting.

The levelling and cleaning of phase data is performed as follows. At first, the large cycle-slips are detected using temporal differences of L_4 with the threshold limit set to 20 TECu/min. Then, each clean part of an arc longer than 15 min is leveled according to Equation (1). In the case of the shorter periods, which are characterized by corrupted phase data, they are replaced with a five-epoch moving average of $-P_{4(k)}$. This process slightly smooths the pattern of structure in the time domain, but the values that are derived in such way can be still a good approximation of ionospheric variations. According to our tests, the standard deviation of differences between the applied moving average and raw phase data is at the level of 2 TECu, while the periods of frequent cycle-slips are mostly related to STEC enhancement exceeding 20 TECu. Finally, due to the high threshold limit, we examine the leveled phase measurements using the median of differences between them and the five-epoch averaged code data in 15-min periods. If the absolute values of this indicator are higher than six TECu, what corresponds to three σ , the phase data are shifted accordingly.

The next step of the algorithm is the extraction of patch signatures from clean arcs of L_4 data. According to our preliminary results given in [37], this can be effectively performed with an iterative fitting of a fourth-order polynomial in a three-step procedure. The starting point involves a shift of the L_4 time series to set their minimal values to 0.2. Subsequently, the initial fitting with unit weights is performed. If the maximal difference between the L_4 values and fitted polynomial does not exceed three TECu, the background STEC assessment process is terminated. In the opposite case, the polynomial coefficients are estimated in a two-step iterative mode, removing epochs with differences higher than 1.5 TECu. These repetitions are performed with weights equal to $1/L_4$. The first step is related to iterative fitting only, and enables the application of appropriate weights. They, in turn, are responsible for the faster convergence of polynomial fitting to background STEC variations, which correspond to sub-daily changes of ionospheric conditions and the impact of the elevation angle. The initial fitting provides the preliminary information on the background ionosphere, and is treated as final for very small variations in the magnitude of STEC. The last two-step iterative mode allows the approximation of background STEC level for disturbed conditions. In comparison to earlier analysis aimed at the detection of different ionospheric structures [37], the thresholds applied here are highly restrictive. This corresponds to the results of Polar Cap Products (<https://www.mn.uio.no/fysikk/english/research/projects/swarm/>), which indicated the occurrence of weak patches during the test period (an example of such structures is given in Section 4). Finally, the relative STEC values are computed as a difference between geometry-free data at a particular epoch and the fitted polynomial.

The above algorithm was applied to GNSS data with an elevation mask set to 10° and arcs longer than three hours. The second criterion ensures the proper work of the algorithm and prevents a situation wherein the patch or their sequence could fill the entire time series. As the low-elevated data are expected to be less accurate, the main part of multi-station analyses was performed with the cut-off angle set to 30° .

Figure 1 depicts the performance of the algorithm, including three-step fitting, for an L_4 time series from the northern and southern hemispheres (left and right column, respectively). The first panel (station ALRT, satellite GPS 31) depicts the situation with signatures of patches observed for low-elevated data. In this case, the structures are properly extracted from the L_4 time series, although the orientation of the GNSS signal was poor. On the other hand, it should be remarked that STEC enhancement for almost horizontal direction may significantly differ from the vertical one due to the long path of the signal in the ionosphere.

The remaining arcs that are shown in Figure 1 correspond to the period with extreme patch activity. Comparing the results for the northern (station SRMP, satellite GPS; 32, bottom left panel) and southern hemispheres (station CAS1, satellites GPS 5 and GLONASS; six top and bottom panels on the right side, respectively), one can observe the significant difference in STEC enhancement, which is discussed in detail in Section 4.2. Furthermore, Figure 1 indicates two issues related to the algorithm results. The first is artificial convexity in a fitted polynomial, which is clearly observable in top right

panel. It mostly occurs for elevation below 30° , and in particularly adverse conditions (partially outside extended structures), it may lead to the overestimation of relative STEC values. The application of an appropriate mask practically eliminates it from the final solution. The second effect, which is depicted in results for the southern hemisphere, is the lack of simple dependence of the STEC enhancement on the elevation angle. Comparing figures in the right panel, one can see that the strongest effect (up to ~ 80 TECu) is observed at 30° and 60° of elevation, respectively. The results for the other structures are even more ambiguous, i.e., the signatures at low elevations are both overestimated and underestimated in reference to high-elevated data. This effect is related to the different spatial orientation of GNSS signals. The similar analysis for other periods confirms the independence of an applied indicator on the elevation angle; thus, further analyses used relative enhancement in a slant direction.

Although the work is aimed at the feasibility of GNSS-based patch detection, the presented experiment involved processing data obtained from ~ 180 and ~ 60 permanent stations located in northern and southern hemispheres, respectively (Figure 2). The extension of the analyzed area provides a better preliminary view of ionospheric conditions and, in some cases, allows the explanation of interhemispheric differences. The receivers that were used for patch detection, which had an altitude-adjusted corrected geomagnetic (AACGM) latitude higher than 75° , were marked with red dots for clarity of presentation. The utilized stations belonged to the International GNSS Service (IGS), EUREF Permanent Network (EPN) or participate in Plate Boundary Observatory (PBO) mission. The investigations are based on multi-GNSS (GPS + GLONASS) measurements, but it should be noted that only a few polar stations are equipped with two-constellation receivers. Figure 2 highlights the inequality between the distributions of receivers in both hemispheres, which are connected through land mass configuration. However, analyzing only the polar cap areas, the coverage of the northern part seems to be only slightly better due to the shorter distance of the Greenland stations from the north geomagnetic pole and larger number of stations for this area.

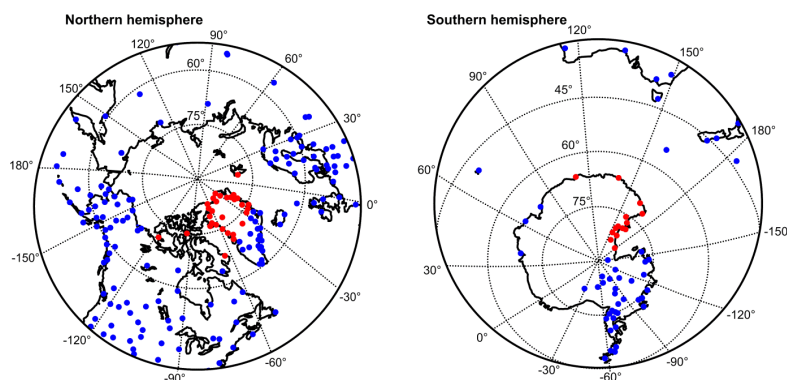


Figure 2. Distributions of GNSS permanent stations in both hemispheres (as seen from geomagnetic poles). Stations that were located over 75° of altitude-adjusted corrected geomagnetic (AACGM) latitude were depicted with red dots.

3. Test Period

In order to evaluate the applicability of relative STEC values, we have analyzed the period of 17–19 March 2015, involving the main and recovery phases of the St. Patrick's Day storm. The selected event was the first extremely strong storm of 24 solar cycle, and is sometimes classified as a super storm. As reported in [44], its source was coronal mass ejection (CME) associated with a C9.1 flare and series of radio bursts. The interplanetary CME arrived at Earth at 4:48 UT, and caused a sudden storm commencement (SSC), which had positive signature exceeding 60 nT that were clearly observed in SYM-H variations (Figure 3). The main phase of the storm can be divided into two intervals of strongly negative IMF. The first of them caused a rapid decrease of the SYM-H index to -101 nT ($\sim 9:30$ UT). After a short-lasting period of positive IMF B_z , the following reorientation initiated the second phase of the storm. This part was related to the magnetic cloud field, and dipped the SYM-H index to

−234 nT (~22:50 UT) [44,45]. During both of these phases, the auroral electrojet (AE) index was at the elevated levels with maxima at ~9:00 and ~13:30 UT, respectively. Furthermore, the increased particle precipitation resulted in an equatorward expansion of the auroral oval to ~60° and ~50° of the geomagnetic latitude on the dayside and nightside, respectively [46]. In the next days, one could observe the extensively elongated recovery phase, which lasted until 25 March 2015.

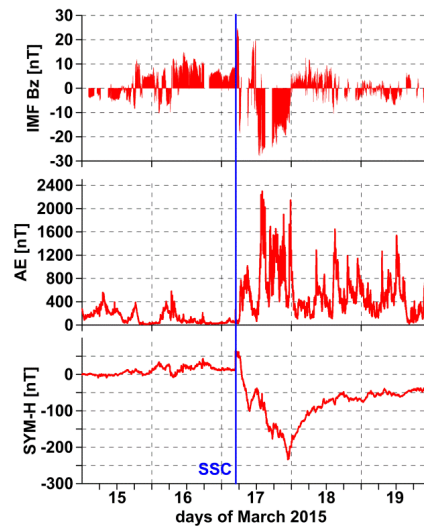


Figure 3. Time series of the selected geomagnetic indices during 15–19 March 2015 (based on OMNI database: <http://omniweb.gsfc.nasa.gov>).

Due to the extreme conditions, this storm has been an object of intensive studies covering all of the regions of the ionosphere. In specific, in [47], the authors used multi-instrumental observations (ground-based and satellite GNSS, ionosondes, altimetry data, and in situ plasma density) to analyze the response of the ionosphere on a global scale. These results demonstrated the positive effect of the storm, which occurred during its entire main phase. They also revealed the significant depletion of ground-based VTEC on 18 March 2015. This pattern for days 17–18 March 2015 was confirmed in [48,49], showing the variations of global/regional electron content (GEC, REC) and regional TEC mapping, respectively. Furthermore [48] demonstrated the interhemispheric asymmetry of VTEC with larger values in the southern part. With regard to high latitudes, the studies reported the growth of scintillations associated with the occurrence of polar patches and auroral blobs during the main phase of the storm [50,51]. The plasma source of these structures (SED) was observed at the equatorward edge of the ionospheric through TEC fluctuation maps as well [46].

4. Results and Discussion

The analysis presented below consists of two parts, and involves three consecutive days (17–19 March 2015). The first part is particularly aimed at the impact of the spatial distribution of the permanent receivers on the feasibility of interhemispheric patch detection. It also demonstrates the comparison of GNSS results with Polar Cap Products based on SWARM in-situ measurements. The second one provides an analysis of the temporal variations of patch occurrence and its dependence on IMF Bz. Furthermore, it includes also a comparison of the STEC enhancement that was observed for both hemispheres. All of the computations were performed with the use of multi-purpose ionosphere monitoring software (IONMON), which was written in Fortran and developed at UWM.

4.1. The Feasibility of Patch Monitoring Using Ground-Based GNSS Receivers

According to the distributions of permanent GNSS receivers in both hemispheres as given in Figure 2, it seems to be clear that the polar patches should, at least to some extent, be detectable. Thus, the starting point is the analysis of the spatial distribution of epoch-wise relative STEC values.

In order to evaluate the ground-based GNSS measurements, they were combined with the plasma density that was derived from SWARM. This satellite mission of the European Space Agency consisted of three LEO satellites: Alpha (A), Bravo (B), and Charlie (C). SWARM A and C fly side by side on a nearly circular orbit with an inclination of 87.35° at an altitude of 462 km. The parameters of the SWARM B orbit are 87.75° and 510 km, respectively. The same instruments are installed onboard each satellite, which allowed precise in situ measurements of the Earth's magnetic field, upper atmosphere, and ionosphere, with high temporal resolution [52]. The dataset provided by this constellation is currently an object of intensive investigations. In our work, we adopted the results of the Polar Cap Products (PCP) project founded by European Space Agency and handled by Department of Physics at the University of Oslo (<https://www.mn.uio.no/fysikk/english/research/projects/swarm/>), which is acknowledged. The main goal of the PCP was the proposal and further application of an algorithm aimed at an automatic detection of polar patches using data from SWARM Langmuir probes. Its results, covering over four years, include foreground and background plasma densities that were derived using the percentile filtering technique, and are available at the site of the project [6].

The comparison of patch detection using both methods is presented in Figure 4. It demonstrates the distributions of relative STEC values and SWARM data as a function of UT and modified AACGM latitude. The latter parameter corresponds to the point of latitude being a projection of real observations on the noon–midnight axis of magnetic local time (MLT). Despite some disadvantages related to a lack of distinction between the dusk and dawn sides, such an approach allows the depiction of the spatial distribution of measurements as well as its daily temporal modification. At this stage, we used only the data with an original AACGM latitude higher than 77° , which is consistent with the methodology that was employed in [6]. The conversion of GNSS data to an MLT-AACGM latitude reference frame was performed with the methodology proposed in [53] using an ionosphere single-layer model (350 km). At this point, we set the cut-off angle at the level of 30° . The SWARM dataset was preprocessed in a similar manner; however, in Figure 4, only the points with a density ratio higher than two were given.

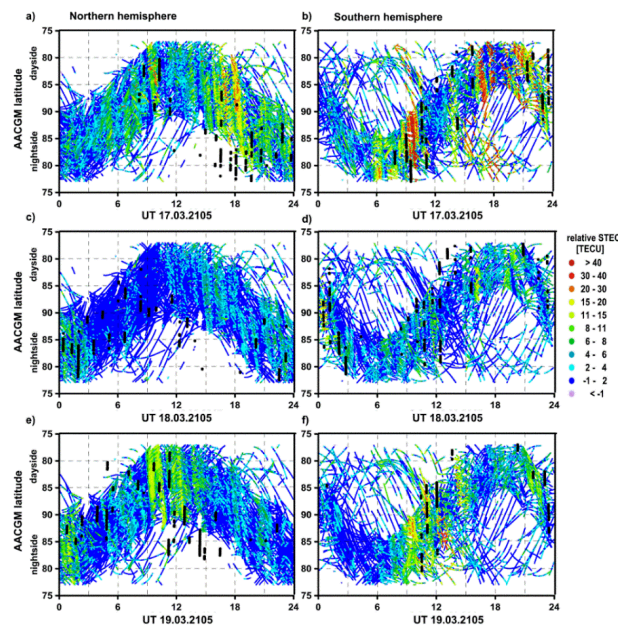


Figure 4. The comparison of patch detection using GNSS-based relative STEC values and SWARM in situ data (black dots). AACGM latitudes are derived with the projection of measurement points onto the noon–midnight axis of magnetic local time (MLT). Only the points with a density ratio higher than two are shown in the case of SWARM data.

Looking firstly only at the spatiotemporal distribution of ground-based GNSS data, one can assume that the application of epoch-wise relative STEC values enables tracing patch convection

across the polar cap. Comparing Figures 2 and 4, it is clear that this feasibility is mostly related to the sub-network of receivers that are located in the Greenland and Transantarctic mountains, respectively. They provide the majority of ionospheric samples, which correspond to the rotating bands observed in Figure 4. The zone in the northern hemisphere is wider due to the better meridional spread and distribution of the permanent stations. The situation in the southern part is slightly worse. The distance between the Transantarctic mountains implicates the restriction of the sounded area to $\sim 85^\circ$ of AACGM latitude. On the other hand, the singular receivers that are located on the coastline of Antarctica (see Figure 2) provide some information at the opposite side of the polar ionosphere, which may be useful for the detailed study of patch convection. This feasibility is predominantly visible for the strongest structures on 17 March 2015. The interhemispheric comparison of patch signature continuity confirmed the more favorable measurement conditions near the North Pole. Almost all of the structures that are detected there are observed for the entire 10° band of modified AACGM latitude. Moreover, even very weak patches with STEC enhancement at the level of a few TECu appear to be correctly identified. The continuity of signatures is not always the case for the southern hemisphere (e.g., 19:00–22:00 UT in Figure 4b or 12:00–14:00 UT in Figure 4f). This discrepancy between both areas seems to be related to the difference in the receiver distributions in the Greenland and Transantarctic mountains. The approximately linear shape in the second case may influence patch tracing. One can assume that the parallel orientation of the GNSS sub-network and patch propagation is advantageous (all of the stations sequentially observe the particular structure), whereas in perpendicular exposure, simultaneous detection is expected. Thus, in such a case, the effectiveness of the GNSS technique depends on the current satellite constellation, which under very adverse conditions may not be achieved. This unfavorable distribution of stations is probably also responsible for the blurring of structures that was detected near the South Pole.

The noteworthy findings are provided by the comparison of patch detection with ground-based GNSS and SWARM data. Looking at Figure 4, one can observe that the results for both methods are only partially compliant. For some periods—such as 16:00–20:00 UT as presented in Figure 4a or 10:00–12:00 UT as given in Figure 4f—there is a good coincidence, but this is not always the case. The main reasons for discrepancies are the orientation of SWARM orbits and the sounding of different areas of the polar ionosphere by both techniques. In order to depict both of these effects, we selected two representative examples. The first of them, which is given in Figure 5, is related to the sequence of three patches (~ 60 – 90 TECu in a slant direction) that occurred in the southern hemisphere during the main phase of the storm (16:30–17:40 UT on 17 March). The top panel of Figure 5 presents the relative STEC values as a function of MLT and AACGM latitude, with the latter extended to 60° and traces of two arcs of SWARM satellites. The bottom one provides the temporal variations of foreground plasma density for the SWARM series. Analyzing these results, it should be remarked that the auroral oval for this period was extended to 60° [46]. As is shown, both techniques allow the identification of extreme structures, and the results are compatible. In the case of LEO satellites, the detection occurs at 70 – 73° of AACGM latitude, i.e., below the latitudinal limit as applied for automatic detection equal to 77° [6]. Thus, these structures were not classified as patches in such a mode of processing. Certainly, it does not reduce the effectiveness of the SWARM results, but rather highlights that the monitoring of the polar ionosphere for the particular passage of an LEO satellite depends on its orbit orientation and the area that was adopted for patch detection. In contrast to this, the distribution of GNSS measurements was in this case highly favorable, as it resulted in a clear depiction of high-density plasma on the dayside ionosphere. Figure 5 confirmed that the usefulness of ground-based GNSS data at the southern hemisphere is mostly restricted to polar cap area.

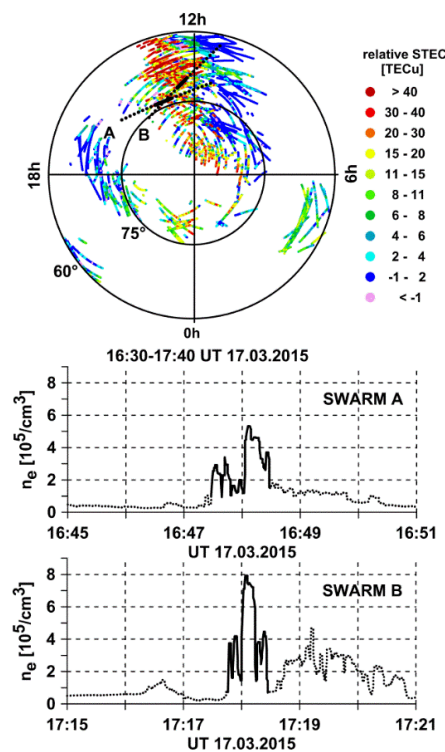


Figure 5. The signatures of patches derived from GNSS and SWARM measurements. The top panel presents the distribution of relative STEC values as a function of magnetic local time (MLT) and AACGM latitude with two superimposed arcs of SWARM depicted with black dotted and solid lines. The bottom panel presents the corresponding temporal profiles of SWARM foreground plasma density. The strong enhancements of plasma density are marked with a solid black line in both panels.

Figure 6 clarifies the opposite situation with patches detected only in SWARM data (Figure 4c, 4:00–10:00 UT). As it was reported in previous investigations, this period was characterized by a deep depletion of plasma [47,49]. Due to the same reason and northwardly-oriented IMF, the patches observed in the in situ data are much weaker, as depicted in the bottom panel of Figure 6. In this case, the solid black lines correspond to patch signatures according to PCP results. Looking at the results for elevation mask equal to 30° , it is clear that GNSS and SWARM techniques sounded different parts of the ionosphere. Thus, the lack of consistency that is observed in Figure 4c is a consequence of the visualization method. On the other hand, this highlights the possible scenario wherein GNSS measurements do not capture the propagated structures. Taking into account the distribution of receivers, it is likely to occur for periods with the most data on the dusk or dawn sides. This effect is partly related to the equatorward orientation of GNSS signals that resulted from the applied elevation mask. Hence, the right top panel of Figure 6 demonstrates the results, including the low-elevated data ($>15^\circ$). As one can expect, this improves the coverage of the polar area by GNSS measurements, and allows the detection of the first structure observed in SWARM data. Its signature for relative STEC values reaches up to six to seven TECu. The second patch was not identified with GNSS, which may be related to the still poor distribution of ground-based measurements, as well as the extremely weak enhancement in this case. According to the results of the PCP project, this structure met the foreground/background criterion, but the relative growth of plasma density was only at the level of $0.2 \times 10^5/\text{cm}^3$. The identification of such a low-density patch with GNSS seems to be questionable, and needs further investigation.

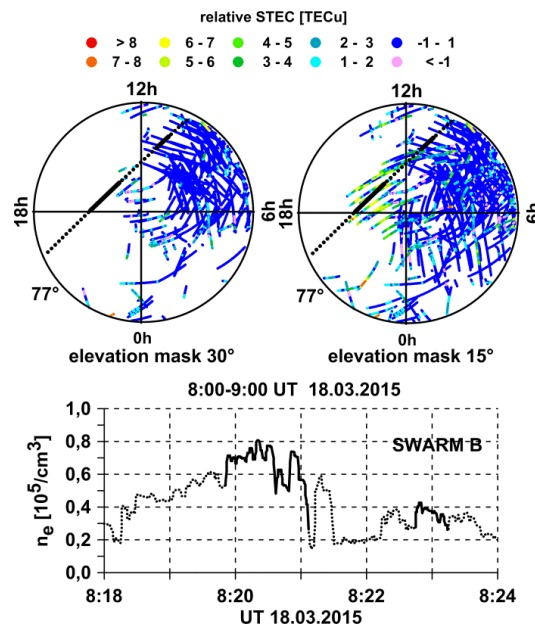


Figure 6. The signatures of patches derived from GNSS and SWARM measurements for a depleted ionosphere. The top panel presents the distribution of relative STEC values as a function of MLT and AACGM latitude for elevation masks equal to 30° and 15° with a superimposed arc of SWARM data (denoted with dotted and solid black lines). The bottom panel presents temporal profile of SWARM foreground plasma density. Black solid lines correspond to patch structures according to the Polar Cap Products (PCP) project.

Summarizing the above, the relative STEC values can be treated as an alternative for current methods of polar patch detection. Taking into account the current distribution of GNSS receivers, the proposed methodology allows the identification and tracking of polar patches. On the other hand, the comparison of GNSS and SWARM data indicates that both of these techniques may not provide the complete ionospheric information. Thus, their integration seems to be an appropriate technique for more detailed study.

4.2. The Analysis of Patch Occurrence with Relative STEC Values.

The results given in Figure 4 confirmed the feasibility of continuous patch detection with GNSS data. Thus, this section presents the analysis of these structures' occurrence during the following phases of the storm and its dependence on IMF Bz. Due to the difference in GNSS data distributions for both hemispheres, we performed this analysis for 3° bands of modified AACGM latitude, according to scheme given in Figure 7. Although the selected areas are not homogenous, which may influence the results to some extent, they provide continuous observations in both cases.

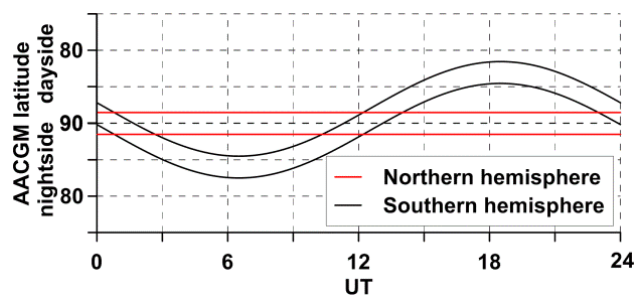


Figure 7. Sectors used for patch analysis.

The summary of such prepared results is demonstrated in Figure 8. It integrates the variations of IMF Bz derived from the OMNI database (top panel) and the epoch-wise maximal values of relative STEC for selected sectors (middle and bottom panels). At this stage, we set the elevation cut-off angle to 30° . The results of analysis were also supported by VTEC values derived from hourly global ionospheric maps (GIM) generated by the European Space Operations Center (ESOC) [54]. The first of them—0.5 VTEC at the pole—was used as an indicator of patch occurrence. Assuming the lack of geometrical dependency of STEC enhancement, this threshold can be identified as the foreground to background ratio for the GNSS technique at the level of 1.5. According to our preliminary comparison with the SWARM dataset, it roughly corresponds to cases when the ratio of plasma density is equal to 2. The latter values show VTEC on the dayside ionosphere at 50° , 60° , and 70° of the AACGM latitude, respectively.

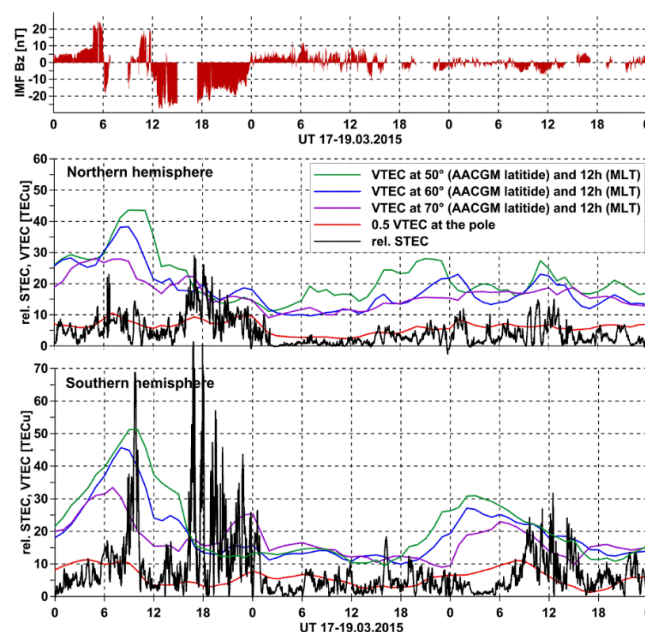


Figure 8. Variations of IMF Bz (top panel) and maximal relative STEC values for sectors given in Figure 7 (middle and bottom panels). In the latter case, VTEC on the dayside ionosphere and at the poles are superposed.

Analyzing the occurrence of polar patches on 17 March 2015, one can observe two periods of high patch activity, i.e., $\sim 6:00\text{--}10:00$ UT and $\sim 16:00\text{--}24:00$ UT. Both of them correspond to negative IMF Bz, which is consistent with the current knowledge in this field [7,17]. In the case of the first period, the structures near the North Pole rarely exceeded 10 TECu. However, the much more intense patches, ~ 30 TECu, were detected for low-elevated GNSS data (Figure 9). This confirms the feasible and adverse impact of data distribution on the derived results. Taking into account the low-elevated data, the structures that were observed in the first phase reached over 30 TECu and 60 TECu in the northern and southern hemispheres, respectively. In both cases, the strongest enhancement was related to the sequence of three patches ($\sim 8.30\text{--}10.30$ UT), for which propagation above the North Pole is clearly depicted in Figure 9. For the southern hemisphere (the middle panel of Figure 8), the two first structures are merged due to the difference in signatures for particular satellites. The corresponding disproportion for both analyzed regions is also observed in the SWARM data set, provided that not all of the structures have been classified as patches due to the mentioned latitudinal mask. This patch activity appears to be related to high level of dayside plasma (depicted in Figure 8 as VTEC) and feeding of polar ionosphere with the rapid extension of the auroral oval that was reported in [46]. The interhemispheric comparison of dayside VTEC from GIM does not explain such strong differences in patch enhancement. The concentration of plasma in the southern hemisphere is only slightly

higher (up to 10%), whereas the last structure observed there was approximately two times stronger. This inconsistency is probably related to the infeasibility of the detection of polar structures with hourly GIM.

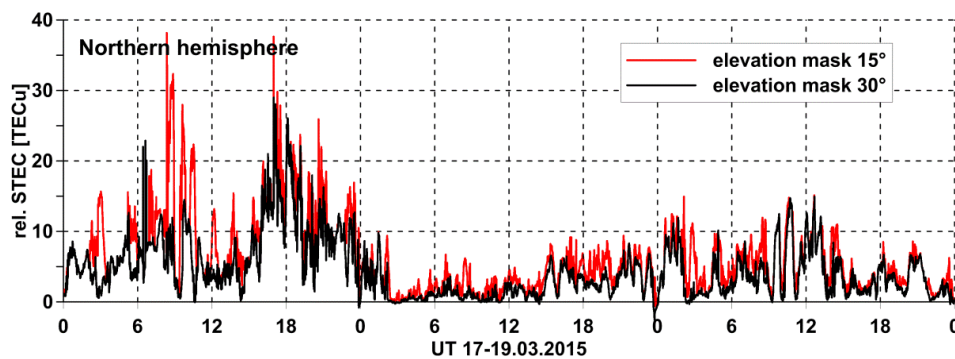


Figure 9. Variations of maximal relative STEC values according to the northern hemisphere sector given in Figure 7, as derived for two employed elevation cut-off angles.

The second period (~16:00–24:00 UT on 17 March 2015) with an accumulation of large-scale structures confirms the disparity of enhancement observed for both hemispheres. In this case, the maximal STEC values for the southern hemisphere were almost three times the size of those of the northern hemisphere. Unfortunately, the large number of structures leads to their strong merging. This effect requires further investigation, but it should be able to be reduced through the selection of particular satellites. On the other hand, this period can be considered as the best-case scenario with reference to the number of samples on the dayside ionosphere. Thus, in order to clarify the interhemispheric differences, we used the relative STEC values derived from all of the stations given in Figure 2. Such results (Figure 10), covering AACGM latitudes above 45° , clearly demonstrate the propagation of plasma being a source of polar patches. As one can see, the stream on the northern hemisphere was characterized by relative STEC enhancement rarely exceeding 20 TECu, whereas on the opposite side, it reached 40 TECu and more. Taking into account the spatially extended effect in the second case, one can assume that the observed disproportion in polar structures is a consequence of the difference in the dense stream of dayside plasma. The second sequence of patches seems to be originated from the same region of high-density plasma as the first; however, it was fed from the dusk sector of the mid-latitude ionosphere. This also explains the relatively low level of noon VTEC for this period. The much less intense patches between ~10:00 and 16:00 UT resulted from the reorientation of IMF Bz, changing the high-latitude convection pattern, and the poleward shift of auroral oval. The single structures that were observed within are a few times weaker, and did not exceed 15 TECu.

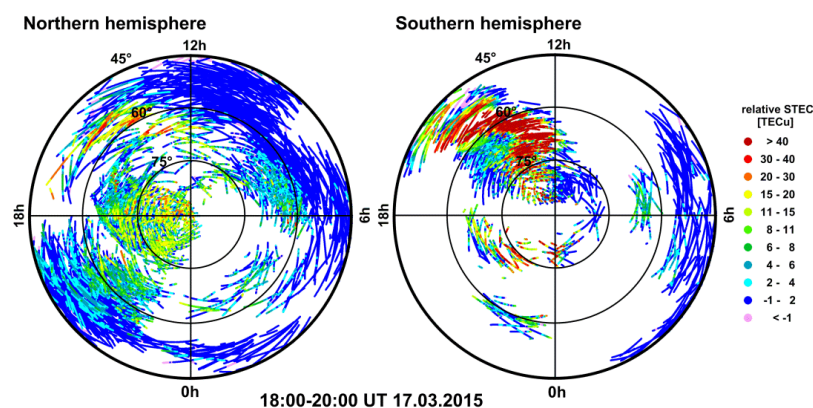


Figure 10. The distribution of relative STEC values as a function of AACGM latitude and MLT obtained for both hemispheres (18:00–20:00 UT on 17 March 2015).

The occurrence of patches in the two periods indicated above is basically consistent with the regional maps of the ionosphere that were provided in [50], which were generated using MAP GPS software [55]. However, the structures that were observed in the latter case featured VTEC not exceeding 20 TECu. This difference seems to be related to two factors. The first of them is STEC–VTEC conversion, which reduces the enhancement for low-elevated observations. The second reason is the applied indicator. We adopted the maximal epoch-wise STEC values, while the VTEC values for each of the 1° by 1° bins in [50] are the results of adjustment.

The opposite conditions were observed for the period ~00:00–14:00 UT on 18 March, which were characterized by northwardly-oriented IMF and a depleted ionosphere. The results for the northern side depicted an extremely quiet ionosphere (Figure 8), which was partly related to poor data distribution. The application of additional low-elevated data revealed the occurrence of four patches with STEC enhancement at the level of five to seven TECu (Figure 9). These met the applied criterion and were classified as patches in the SWARM data as well. On the other hand, it should be remarked that for such a depleted ionosphere, the other structures may fulfill this condition, and be improperly classified as patches. This seems to be especially important for GNSS data, in which the total amount of plasma in the slant direction is measured. Similar to the southward IMF case, the structures in the southern hemisphere were stronger and reached up to 10 TECu. More interestingly, these structures were also observed on the nightside (Figure 4). The results for the further part of the recovery phase depicted another sequence of patches (~8:00–16:00 UT on 19 March), which occurred for slightly negative IMF Bz. Although the structures were much weaker (up to 15 TECu and 30 TECu in the northern and southern hemispheres, respectively), their generation seems to be similar to the second sequence observed during the storm. According to Figure 8, these patches are probably related to the enhancement of VTEC that was observed at noon mid-latitudes about six hours earlier. Unfortunately, the unfavorable data distribution in the southern hemisphere prevents the more detailed evaluation of ionospheric conditions in this case.

5. Conclusions

This contribution evaluated the applicability of ground-based GNSS measurements for the continuous detection of polar patches. In contrast to earlier analyses performed with regional TEC mapping, this study takes advantage of epoch-wise relative STEC values. The adopted indicator represents the point information on STEC enhancement and allows the efficient monitoring of structures in the polar area. Furthermore, its definition enables the common processing of data from a network of GNSS stations and provides maps of ionospheric irregularity occurrence.

The analysis of current spatial distribution of GNSS data in the polar regions indicates the feasibility of patch monitoring with the proposed technique. As it was shown, the signatures of structures with STEC enhancement at the level of a few TECu can be easily detected. Nevertheless, the efficiency of the proposed methodology is restricted by the distribution of permanent stations and the land mass configuration. Thus, most of the samples cover one sector of the polar ionosphere, and, according to the given comparison with SWARM in situ data, may not provide the full view of ionospheric conditions. On the other hand, if both techniques sounded the same part of the ionosphere, their results were consistent. The undoubted advantage of ground-based GNSS data is better spatial coverage, which allows the tracking of patch propagation.

The results also depict the applicability of the GNSS technique for the continuous interhemispheric comparison of analyzed structures. In the case of the St. Patrick's Day storm and its recovery phase, the patches were observed simultaneously in both hemispheres. However, they were characterized by a strong disproportion of plasma enhancement. According to the presented investigations involving mid-latitudes as well, the reason for discrepancy is the denser tongue of ionization in the southern hemisphere. In the analyzed period, the more intense structure was observed for southwardly oriented IMF Bz, which confirms the previous conclusions. For the opposite case, the structures were significantly weaker.

Finally, it is believed that epoch-wise ionospheric information from ground-based GNSS receivers represent an interesting alternative for the other methods of patch monitoring. Our preliminary comparison with SWARM data indicated that the integration of different data sets should enable more comprehensive studies.

Author Contributions: Conceptualization of the manuscript idea, R.S.; Methodology and Software, R.S.; Investigations, R.S. and J.P.; Writing-Original Draft Preparation, R.S.; Writing-Review & Editing, J.P.; Supervision and Funding Acquisition, J.P.

Funding: This research was funded by the National Science Centre, Poland, grant number 2016/23/D/ST10/01546. The APC was funded by University of Warmia and Mazury in Olsztyn.

Acknowledgments: The authors are grateful for GNSS data and products provided by IGS/EPN, ESOC and UNAVCO. We acknowledge use of NASA/GSFC's Space Physics Data Facility's OMNIWeb service and OMNI data. We also acknowledge use of Polar Cap Project data founded by ESA and realized by Department of Physics, University of Oslo.

Conflicts of Interest: The authors declare no conflict of interest

References

1. Bowline, M.D.; Sojka, J.J.; Schunk, R.W. Relationship of theoretical patch climatology to polar cap patch observations. *Radio Sci.* **1996**, *31*, 635–644. [[CrossRef](#)]
2. Kullen, A.; Brittnacher, M.; Cumnock, J.A.; Blomberg, L.G. Solar wind dependence of the occurrence and motion of polar auroral arcs: A statistical study. *J. Geophys. Res.* **2002**, *107*, A11. [[CrossRef](#)]
3. Li, G.; Ning, B.; Ren, Z.; Hu, L. Statistics of GPS ionospheric scintillation and irregularities over polar regions at solar minimum. *GPS Solut.* **2010**, *14*, 331–341. [[CrossRef](#)]
4. Carlson, H.C. Sharpening our thinking about polar cap ionospheric patch morphology, research, and mitigation techniques. *Radio Sci.* **2012**, *47*, RS0L21. [[CrossRef](#)]
5. Prikryl, P.; Jayachandran, P.T.; Chadwick, R.; Kelly, T.D. Climatology of GPS phase scintillation at northern high latitudes for the period from 2008 to 2013. *Ann. Geophys.* **2015**, *33*, 531–545. [[CrossRef](#)]
6. Spicher, A.; Clausen, L.B.N.; Miloch, W.J.; Lofstad, V.; Jin, Y.; Moen, J.I. Interhemispheric study of polar cap patch occurrence based on Swarm in situ data. *J. Geophys. Res. Space Phys.* **2017**, *122*, 3837–3851. [[CrossRef](#)]
7. Buchau, J.; Reinisch, B.; Weber, E.; Moore, J. Structure and dynamics of the winter polar cap F region. *Radio Sci.* **1983**, *18*, 995–1010. [[CrossRef](#)]
8. Weber, E.; Buchau, J.; Moore, J.; Sharber, J.; Livingston, R.; Winningham, J.; Reinisch, B. F layer ionization patches in the polar cap. *J. Geophys. Res.* **1984**, *89*, 1683–1694. [[CrossRef](#)]
9. Weber, E.; Klobuchar, J.; Buchau, J.; Carlson, H.; Livingston, R.; de la Beaujardiere, O.; McCreedy, M.; Moore, J.; Bishop, G. Polar cap F layer patches: Structure and dynamics. *J. Geophys. Res.* **1986**, *91*, 12121–12129. [[CrossRef](#)]
10. Krankowski, A.; Shagimuratov, I.; Baran, L.; Epishov, I.; Tepenitzyna, N. The occurrence of polar cap patches in TEC fluctuations detected using GPS measurements in Southern Hemisphere. *Adv. Space Res.* **2006**, *38*, 2601–2609. [[CrossRef](#)]
11. Pedersen, T.; Fejer, B.; Doe, R.; Weber, E. An incoherent scatter radar technique for determining two-dimensional horizontal ionization structure in polar cap F region patches. *J. Geophys. Res.* **2000**, *105*, 10637–10655. [[CrossRef](#)]
12. Coley, W.; Heelis, R. Adaptive identification and characterization of polar ionization patches. *J. Geophys. Res.* **1995**, *100*, 23819–23827. [[CrossRef](#)]
13. Robinson, R.M.; Tsunoda, R.T.; Vickrey, J.F.; Guerin, L. Sources of F region ionization enhancements in the nighttime auroral zone. *J. Geophys. Res.* **1985**, *90*, 7533–7546. [[CrossRef](#)]
14. Crowley, G.; Ridley, A.J.; Deist, D.; Wing, S.; Knipp, D.J.; Emery, B.A.; Foster, J.; Heelis, R.; Hairston, M.; Reinisch, B.W. Transformation of high-latitude ionospheric F region patches into blobs during the March 21, 1990, storm. *J. Geophys. Res.* **2000**, *105*, 5215–5230. [[CrossRef](#)]
15. Jin, Y.; Moen, J.I.; Miloch, W.J. GPS scintillation effects associated with polar cap patches and substorm auroral activity: Direct comparison. *J. Space Weather Space Clim.* **2014**, *4*, A23. [[CrossRef](#)]
16. Lockwood, M.; Carlson, H.C. Production of polar cap electron density patches by transient magnetopause reconnection. *Geophys. Res. Lett.* **1992**, *19*, 1731–1734. [[CrossRef](#)]

17. Sojka, J.J.; Bowline, M.D.; Schunk, R.W. Patches in the polar ionosphere: UT and seasonal dependence. *J. Geophys. Res.* **1994**, *99*, 14959–14970. [[CrossRef](#)]
18. Moen, J.; Carlson, H.C.; Oksavik, K.; Nielsen, C.P.; Pryse, S.E.; Middleton, H.R.; McCreia, I.W.; Gallop, P. EISCAT observations of plasma patches at sub-auroral cusp latitudes. *Ann. Geophys.* **2006**, *24*, 2363–2374. [[CrossRef](#)]
19. Clausen, L.B.N.; Moen, J.I. Electron density enhancements in the polar cap during periods of dayside reconnection. *J. Geophys. Res. Space Phys.* **2015**, *120*, 4452–4464. [[CrossRef](#)]
20. Foster, J.C. Storm time plasma transport at middle and high latitudes. *J. Geophys. Res.* **1993**, *98*, 1675–1689. [[CrossRef](#)]
21. Coster, A.J.; Skone, S. Monitoring storm-enhanced density using IGS reference station data. *J. Geod.* **2009**, *83*, 345–351. [[CrossRef](#)]
22. Rodger, A.S.; Pinnock, M.; Dudeney, J.R.; Baker, K.B.; Greenwald, R.A. A new mechanism for polar patch formation. *J. Geophys. Res.* **1994**, *99*, 6425–6436. [[CrossRef](#)]
23. Oksavik, K.; Ruohoniemi, J.M.; Greenwald, R.A.; Baker, J.B.H.; Moen, J.; Carlson, H.C.; Yeoman, T.K.; Lester, M. Observations of isolated polar cap patches by the European Incoherent Scatter (EISCAT) Svalbard and Super Dual Auroral Radar Network (SuperDARN) Finland radars. *J. Geophys. Res.* **2006**, *111*, A05310. [[CrossRef](#)]
24. Sojka, J.J.; Bowline, M.D.; Schunk, R.W.; Decker, D.T.; Valladares, C.E.; Sheehan, R.; Anderson, D.N.; Heelis, R.A. Modeling polar cap F-region patches using time varying convection. *Geophys. Res. Lett.* **1993**, *20*, 1783–1786. [[CrossRef](#)]
25. Valladares, C.; Decker, D.; Sheehan, R.; Anderson, D.; Bullett, T.; Reinisch, B. Formation of polar cap patches associated with north-to-south transitions of the interplanetary magnetic field. *J. Geophys. Res.* **1998**, *103*, 14657–14670. [[CrossRef](#)]
26. Carlson, H.C.; Oksavik, K.; Moen, J.; Pedersen, T. Ionospheric patch formation: Direct measurements of the origin of a polar cap patch. *Geophys. Res. Lett.* **2004**, *31*, L08806. [[CrossRef](#)]
27. Carlson, C.H.; Moen, J.; Oksavik, K.; Nielsen, C.; McCreia, I.W.; Pedersen, T.; Gallop, P. Direct observations of injection events of subauroral plasma into the polar cap. *Geophys. Res. Lett.* **2006**, *33*, L05103. [[CrossRef](#)]
28. Coley, W.R.; Heelis, R.A. Seasonal and universal time distribution of patches in the northern and southern polar caps. *J. Geophys. Res.* **1998**, *103*, 29229–29237. [[CrossRef](#)]
29. Rodger, A.S.; Graham, A.C. Diurnal and seasonal occurrence of polar patches. *Ann. Geophys.* **1996**, *14*, 533–537. [[CrossRef](#)]
30. Noja, M.; Stolle, C.; Park, J.; Lühr, H. Long-term analysis of ionospheric polar patches based on CHAMP TEC data. *Radio Sci.* **2013**, *48*, 289–301. [[CrossRef](#)]
31. Jakowski, N.; Mayer, C.; Hoque, M.M.; Wilken, V. Total electron content models and their use in ionosphere monitoring. *Radio Sci.* **2011**, *46*, RS0D18. [[CrossRef](#)]
32. Sieradzki, R. An analysis of selected aspects of irregularities oval monitoring using GNSS observations. *J. Atmos. Sol. Terr. Phy.* **2015**, *129*, 87–98. [[CrossRef](#)]
33. Cherniak, I.; Zakharenkova, I. New advantages of the combined GPS and GLONASS observations for high-latitude ionospheric irregularities monitoring: Case study of June 2015 geomagnetic storm. *Earth Planets Space* **2017**, *69*, 66. [[CrossRef](#)]
34. Sieradzki, R.; Paziewski, J. Study on reliable GNSS positioning with intense TEC fluctuations at high latitudes. *GPS Solut.* **2016**, *20*, 553–563. [[CrossRef](#)]
35. Zhang, Q.-H.; Moen, J.; Lockwood, M.; McCreia, I.; Zhang, B.C.; McWilliams, K.A.; Zong, Q.; Zhang, S.; Ruohoniemi, J.; Thomas, E.; et al. Polar cap patch transportation beyond the classic scenario. *J. Geophys. Res. Space Phys.* **2016**, *121*, 9063–9074. [[CrossRef](#)]
36. Durgonics, T.; Komjathy, A.; Verkhoglyadova, O.; Shume, E.B.; Benzon, H.-H.; Mannucci, A.J.; Butala, M.D.; Høeg, P.; Langley, R.B. Multiinstrument observations of a geomagnetic storm and its effects on the Arctic ionosphere: A case study of the 19 February 2014 storm. *Radio Sci.* **2017**, *52*. [[CrossRef](#)]
37. Sieradzki, R.; Paziewski, J. GNSS-based analysis of ionospheric conditions around the North Pole during sequence of geomagnetic storms in March 2012. *EGU Gen. Assembly* **2018**, *20*, 6211.
38. Hernandez-Pajares, M.; Juan, J.M.; Sanz, J. Medium-scale traveling ionospheric disturbances affecting GPS measurements: Spatial and temporal analysis. *J. Geophys. Res.* **2006**, *111*, A07S11. [[CrossRef](#)]

39. Paziewski, J.; Sieradzki, R. Integrated GPS+BDS instantaneous medium baseline RTK positioning: Signal analysis, methodology and performance assessment. *Adv. Space Res.* **2017**, *60*, 2561–2573. [[CrossRef](#)]
40. Sieradzki, R.; Paziewski, J. MSTIDS impact on GNSS observations and its mitigation in rapid static positioning at medium baselines. *Ann. Geophys.* **2016**, *58*, A0661.
41. Nykiel, G.; Zanimonskiy, Y.; Yampolski, Y.; Figurski, M. Efficient usage of dense GNSS networks in central Europe for the visualization and investigation of ionospheric TEC variations. *Sensors* **2017**, *17*, 2298. [[CrossRef](#)]
42. Astafyeva, E.; Yasyukevich, Y.; Maksikov, A.; Zhivetiev, I. Geomagnetic storms, super-storms, and their impacts on GPS-based navigation systems. *Space Weather* **2014**, *12*, 508–525. [[CrossRef](#)]
43. Liu, Z. A new automated cycle slip detection and repair method for a single dual-frequency GPS receiver. *J. Geod.* **2011**, *85*, 171–183. [[CrossRef](#)]
44. Wu, C.-C.; Liou, K.; Lepping, R.P.; Hutting, L.; Plunkett, S.; Howard, R.A.; Socker, D. Earth, The first super geomagnetic storm of solar cycle 24: “The St. Patrick’s day event (17 March 2015)”. *Earth Planets Space* **2016**, *68*, 151. [[CrossRef](#)]
45. Marubashi, K.; Cho, K.-S.; Kim, R.-S.; Kim, S.; Park, S.-H.; Ishibashi, H. The 17 March 2015 storm: The associated magnetic flux rope structure and the storm development. *Earth Planets Space* **2016**, *68*, 173. [[CrossRef](#)]
46. Cherniak, I.; Zakharenkova, I.; Redmon, R. Dynamics of the high-latitude ionospheric irregularities during the March 17, 2015 St. Patrick’s Day storm: Ground-based GPS measurements. *Space Weather* **2015**, *13*, 585–597. [[CrossRef](#)]
47. Astafyeva, E.; Zakharenkova, I.; Förster, M. Ionospheric response to the 2015 St. Patrick’s Day storm: A global multi-instrumental overview. *J. Geophys. Res. Space Phys.* **2015**, *120*, 9023–9037. [[CrossRef](#)]
48. Nava, B.; Rodríguez-Zuluaga, J.; Alazo-Cuartas, K.; Kashcheyev, A.; Migoya-Orué, Y.; Radicella, S.M.; Amory-Mazaudier, C.; Fleury, R. Middle- and low-latitude ionosphere response to 2015 St. Patrick’s Day geomagnetic storm. *J. Geophys. Res. Space Phys.* **2016**, *121*, 3421–3438. [[CrossRef](#)]
49. Krypiak-Gregorczyk, A.; Wielgosz, P.; Borkowski, A. Ionosphere Model for European Region Based on Multi-GNSS Data and TPS Interpolation. *Remote Sens.* **2017**, *9*, 1221. [[CrossRef](#)]
50. Prikryl, P.; Ghoddousi-Fard, R.; Weygand, J.M.; Viljanen, A.; Connors, M.; Danskin, D.W.; Jayachandran, P.T.; Jacobsen, K.S.; Andalsvik, Y.L.; Thomas, E.G.; et al. GPS phase scintillation at high latitudes during the geomagnetic storm of 17–18 March 2015. *J. Geophys. Res. Space Phys.* **2016**, *121*, 10448–10465. [[CrossRef](#)]
51. Jin, Y.; Oksavik, K. GPS Scintillations and Losses of Signal Lock at High Latitudes During the 2015 St. Patrick’s Day Storm. *J. Geophys. Res.* **2018**, *123*, 7943–7957. [[CrossRef](#)]
52. Olsen, N.; Friis-Christensen, E.; Floberghagen, R.; Alken, P.; Beggan, C.; Chulliat, A.; Doornbos, E.; Encarnaçao, J.; Hamilton, B.; Hulot, G.; et al. The Swarm Satellite Constellation Application and Research Facility (SCARF) and Swarm data products. *Earth Planets Space* **2013**, *65*, 1189–1200. [[CrossRef](#)]
53. Shepherd, S.G. Altitude-adjusted corrected geomagnetic coordinates: Definition and functional approximations. *J. Geophys. Res. Space* **2014**, *119*, 7501–7521. [[CrossRef](#)]
54. Feltens, J. Chapman Profile Approach for 3-d Global TEC Representation, IGS Presentation. In Proceedings of the 1998 IGS Analysis Centers Workshop, ESOC, Darmstadt, Germany, 9–11 February 1998; pp. 285–297.
55. Rideout, W.; Coster, A. Automated GPS processing for global total electron content data. *GPS Solut.* **2006**, *10*, 219–228. [[CrossRef](#)]

